Microstructure and Mechanical Properties of Free-Sintering Low Alloy Steel Produced by Three Additive Manufacturing Methods

Thomas Murphy, Christopher Schade, Kerri Horvay
Hoeganaes Corporation
Cinnaminson, NJ 08077

ABSTRACT

The free-sintering low alloy steel was originally designed as a feedstock for binder jet printing applications, where only the finest portion (<25 μm) of the as-atomized particle size distribution is utilized. Since only the fine screen cut is used, the powder cost is high. To improve this economic situation, an investigation was undertaken to expand the market for this dual phase low alloy steel into two additional additive manufacturing processes, thus using a larger percentage of the complete particle size distribution. The additional additive manufacturing processes were laser powder bed fusion, which uses the intermediate particle size (15-53 μm), and directed energy deposition, in which the largest particle size (50-100 μm) is deposited. Also, metal injection molding, a fine powder non-additive manufacturing process, was included to further increase the potential applications for this alloy. By using a larger portion of the particle size distribution with the additional manufacturing methods, the feedstock cost is lowered and the market for the dual phase low alloy steel expanded. The versatility of this dual phase alloy is evident regardless of manufacturing method. Samples produced using all four methods can be intercritically annealed to produce a microstructure and consequently, properties that can be tailored to fit specific application requirements. This is demonstrated with both a range of mechanical properties and metallographic analyses of samples produced by the different methods.

INTRODUCTION

Dual phase (DP) steels are a class of advanced high strength steels (AHSS) having a good combination of strength and ductility. The dual phase microstructures are produced by annealing these low-carbon steels in the intercritical region, $\alpha + \gamma$, of the phase diagram and cooling at a controlled rate. This results in a mixture of soft, ductile ferrite grains and regions of hard, strong martensite and/or bainite. The

proportions of the transformation products are dependent on the intercritical annealing temperature and cooling rate. The annealing temperature controls the amount of ferrite and austenite present and defines the carbon content in the austenite. The combination of transformation products is then determined by the cooling rate.

These alloys are of particular importance because, by changing the intercritical annealing conditions, the balance of the transformation products can be modified, and the resulting properties adjusted to meet specific application demands. More ferrite, which is stable at both annealing and room temperatures, gives a highly ductile, more formable microstructure. The opposite is true by increasing the percentage of austenite and producing a stronger and harder microstructure after cooling. Figure 1 is a chart showing a comparison of several steel families, with the AHSS grades represented by the orange bubbles. The specific bubble indicating the DP alloys range of properties is highlighted with the red arrow.[1]
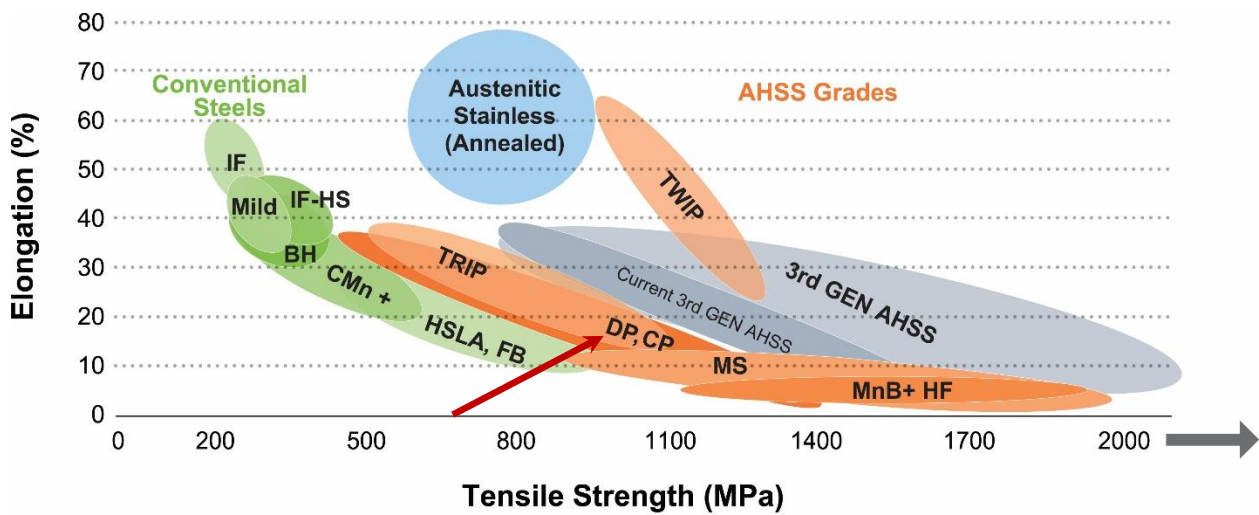
Figure 1. The elongation-ultimate tensile strength comparison of the Advanced High Strength Steel grades. The location of the DP steel properties is indicated by the red arrow.

While the wrought DP alloys have been used successfully in many applications, most notably by the automotive industry for structural body parts, recent efforts have been made to develop a DP steel for use with additive manufacturing (AM) techniques that can meet or exceed the wrought DP properties.[2-4] The hope was to take advantage of the capabilities of AM, including production of more complex parts, and have the ability to customize properties through heat treating. This conversion to using powder-based processes was complicated by several factors. These include the chemical composition of the powder, the need for part densification, and the methods by which the parts are created, including their thermal histories.

In developing a DP steel for use in AM, particularly metal binder jet (MBJ) where the parts require sintering after printing, it was found that powders having the standard wrought DP compositions were incapable of sintering to high densities because they were completely austenitic at the sintering temperature. Commercially available wrought DP alloys are basically Fe + Mn + Si + C alloys and austenitic, face-centered cubic (FCC), during sintering. Because of the FCC crystal structure, they lack sufficient diffusion to create a dense compact after sintering. In contrast, diffusion of the ferritic body-centered cubic (BCC) crystal structure is much greater than the FCC crystal and consequently, a new DP

alloy containing a higher percentage of ferrite stabilizers was developed that would be primarily BCC at sintering temperatures. This new alloy was named Free Sintering Low Alloy (FSLA) and due to the increased amount of ferrite stabilizers, is mostly BCC at the sintering temperatures and capable of sintering to high densities. Figure 2 shows the phase diagrams for a conventional DP600 wrought alloy composition and the new FSLA. As depicted with the sintering window between the red lines, the new alloy is mostly BCC with a small percentage FCC crystal structure at the required sintering temperatures, while the DP600 is completely FCC. The presence of the small portion of FCC with the majority BCC at the sintering temperature has been shown to be ideal for faster and greater densification compared with 100 vol.% ferrite.[5-8]
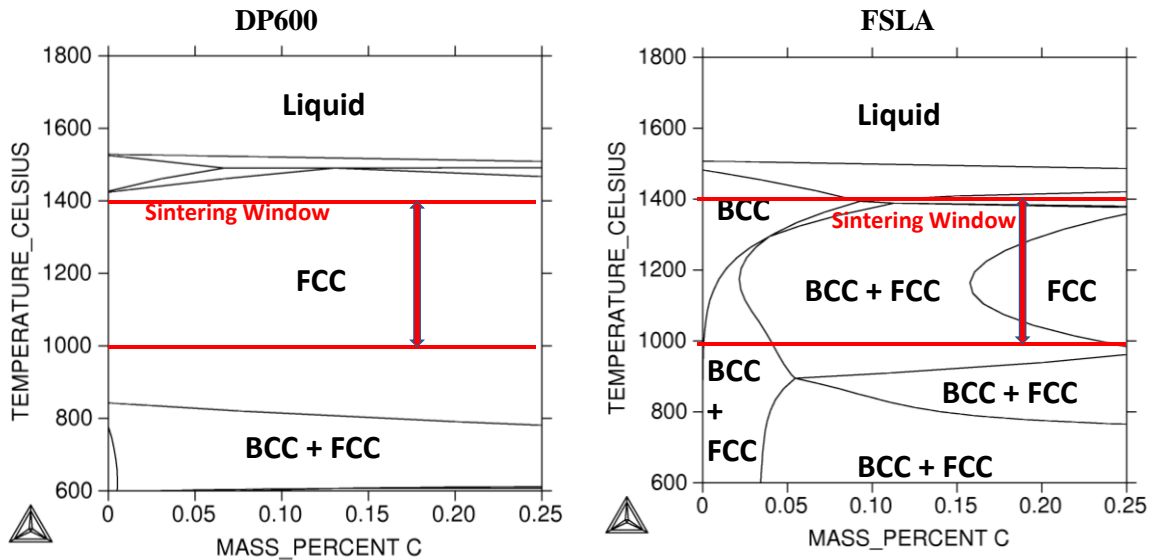

Figure 2. Estimated ThermoCalc phase diagrams for a conventional DP600 alloy and the new FSLA.

As described above, the FSLA composition is compatible with the MBJ process, however it uses only a small portion of the as-atomized particle size distribution (PSD). Figure 3 shows the full distribution of the atomized powder, with the segment used for MBJ shaded in green. Using only this minor amount from the entire PSD, approximately one-third, makes the powder relatively expensive since the remainder of the distribution is unused. To improve this situation and possibly expand powder usage into other powder manufacturing areas, this study was conducted to investigate the applicability of the FSLA to other AM processes, namely both Laser Powder Bed Fusion (LPBF) and Direct Energy Deposition (DED). In addition, Metal Injection Molding (MIM), a non-AM manufacturing method also utilizing a particle size distribution similar to what is used in MBJ, was added to the comparison. This manuscript examines the microstructural changes experienced by samples from the four manufacturing methods by comparing the as-sintered, as-built, and heat treated microstructures using various metallographic techniques. It also shows how mechanical properties change with variations in the proportions of the transformation products.
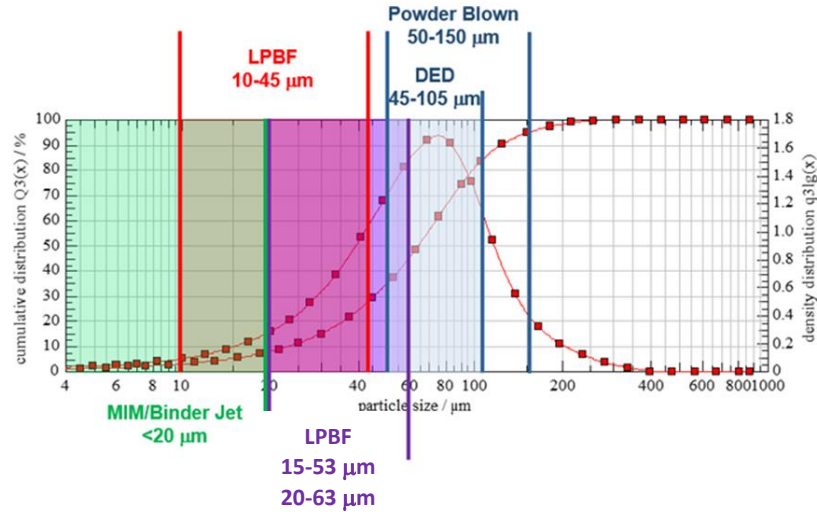
Figure 3. Particle size distribution of gas atomized FSLA powder showing the size ranges used for several AM processes and MIM.

EXPERIMENTAL PROCEDURES

The FSLA powder used in this process comparison was melted in an air atmosphere and atomized using nitrogen. The air melted, gas atomized process produced spherical particles, as seen in Figure 4. The chemical compositions of the FSLA and two commercially available DP steels are compared in Table I. As mentioned previously, the more traditional DP steels are composed primarily of Fe + Mn + Si + C, with Mn, an austenite stabilizer, often as a primary alloying element. In comparison with the FSLA chemical composition, the Mn content of the FSLA alloy is heavily reduced and the ferrite stabilizers, Cr, Mo, and Si increased. This results in an expansion of the high temperature BCC + FCC phase field, resulting in greater densification during sintering. In addition to increasing the compact density, these ferrite stabilizing elements improve the alloy hardenability. Consequently, microstructures containing the stronger transformation products, martensite and bainite, can be attained using slower cooling rates.
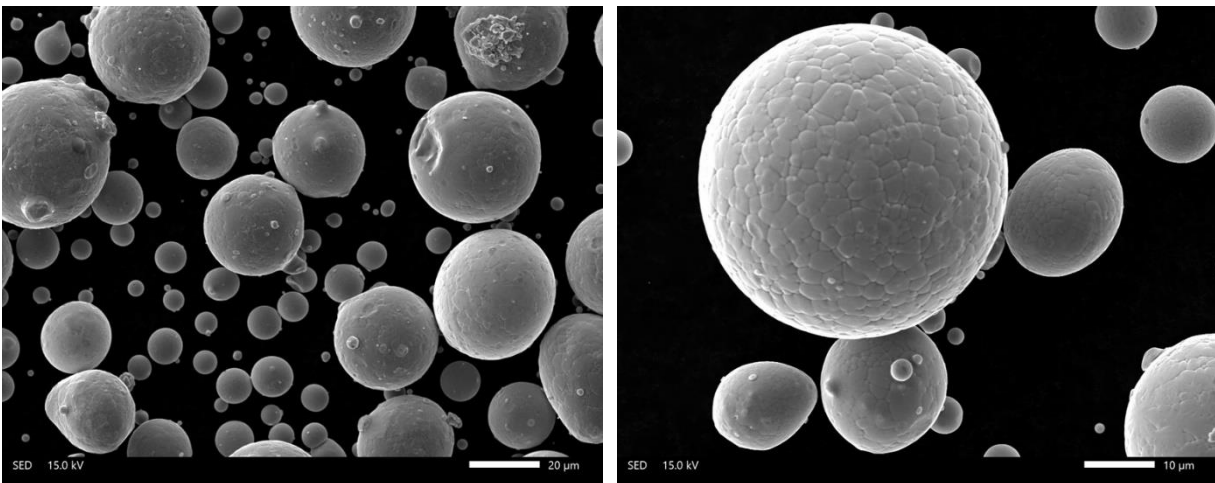

Figure 4. Scanning Electron Microscopy (SEM) Secondary Electron Images (SEI) of the spherical gas atomized FSLA powder for use in LPBF with a size distribution 15-53 μm.

Table I.
Chemical Composition of FSLA and Selected DP Steels[9]

	C	S	Mn	Cr	Mo	Si	V	Nb	Cu
FSLA	0.14	0.007	0.20	1.60	1.45	1.64	0.18	0.18	0.03
DP600*	0.15	0.01	2.5	1.4 Max Total		0.8	Not Added Intentionally		0.2
DP980*	0.23	0.01	2.9	1.4 Max Total		1.0			0.2

* The value following the DP designation refers to the ultimate tensile strength of the alloy in MPa

Samples were manufactured from the FSLA using the three AM processes (MBJ, LPBF and laser DED) and MIM with details from the four shown below. Two of four processes, MBJ and MIM, are basically solid state, with densification occurring during sintering of solid particles. The remaining two, LPBF and laser directed energy deposition (L-DED), are liquid when built with solidification during cooling resulting in the high-density part. This solid vs. liquid state processing affects not only the density of the sample but the microstructures of the two pre-annealed groups are significantly different.

The MBJ samples were printed using a HP Multi Jet Fusion Printer with a water-based binder at a layer thickness of 50 μm. They were sintered at DSH Technologies in MIM3045T furnaces from Elnik Systems. The design of these furnaces allows for debinding and sintering to be completed in one furnace. The samples were sintered at a temperature of 1380 °C (2516 °F) for 30 minutes in a 95 vol.% nitrogen/5 vol.% hydrogen atmosphere.

The MIM samples were prepared with two binder systems, ADVACAT® and ADVAMET®, both supplied by Advanced Metalworking Practices (AMP). Tensile specimens were molded on an Arburg molding machine. Debinding of both sample sets was performed by DSH Technologies and weight loss measurements were made prior to sintering to ensure proper debinding. Sintering was also performed at DSH Technologies using the same procedures as the MBJ samples.

An EOS M290 AM machine, with build dimensions of 250 mm by 250 mm by 325 mm, was used to make the LPBF specimens by melting the FSLA powder layer by layer with an Yb fiber laser (400W) within an argon filled chamber. A constant powder layer thickness was used, with the laser power, scanning speed, and hatch distance varied to find the optimal energy density for the FSLA powder. Once these variables were optimized, a set of standard settings was used to build the mechanical testing specimens in the Z direction. Samples were cut from the build plate in the as-built condition.

L-DED specimens were produced using an Optomec MTS 500CA system equipped with a 1 kW Yb-doped fiber laser (IPG Photonics; λ = 1070 nm) with a spot size of 700 μm and a nozzle standoff distance of ≈8 mm. All samples were fabricated using a laser power of 500 W, traverse speed of 12 mm/s, hatch spacing of 0.4 mm, layer thickness of 0.6 mm, and a powder feeder setting of 6 RPM. Each build cycle was executed under a fully enclosed argon atmosphere with a measured oxygen content <20 ppm. Each layer consisted of an in-fill using a 90-degree alternating hatch approach. No boundary layers were deposited. Mastercam Mill 2019 software, coupled with a proprietary L-DED add-on, was utilized to slice the 3D models and generate the required toolpaths. Builds were fabricated on 1040 steel substrate plates that were solvent degreased and abrasive grit-blasted with 300 μm zirconia shot prior to use.

Intercritical annealing was performed on the samples after sintering and building. Temperatures for the annealing cycle were chosen from the CALPHAD generated equilibrium graph in Figure 5. The FSLA composition was used as the basis for this graph, which shows the relative weight percentage of each phase and compound at temperatures up to ≈1650 °C (≈3000 °F). Using the graph, the relative

proportions of austenite and ferrite can be predicted at each temperature. The deviations from the nearly straight yellow and gray horizontal lines indicate the location of the two-phase field and the rise and corresponding fall of the lines show the estimated relative amounts of ferrite and austenite at each temperature. For instance, the sample is estimated to be ≈95 vol.% ferrite (yellow line) and ≈5 vol.% austenite (gray line) until reaching ≈870 °C (≈1600 °F), where the percentage of ferrite drops to ≈10 vol.% at ≈1150 °C (≈2100 °F) and the austenite increases to ≈90 vol.%. At this temperature, the amount of austenite is maximized, and the ferrite minimized. At temperatures between these austenite/ferrite minimum/maximum values, varying proportions of the two phases can be generated, thus changing the room temperature combination of transformation products and subsequently, the properties.
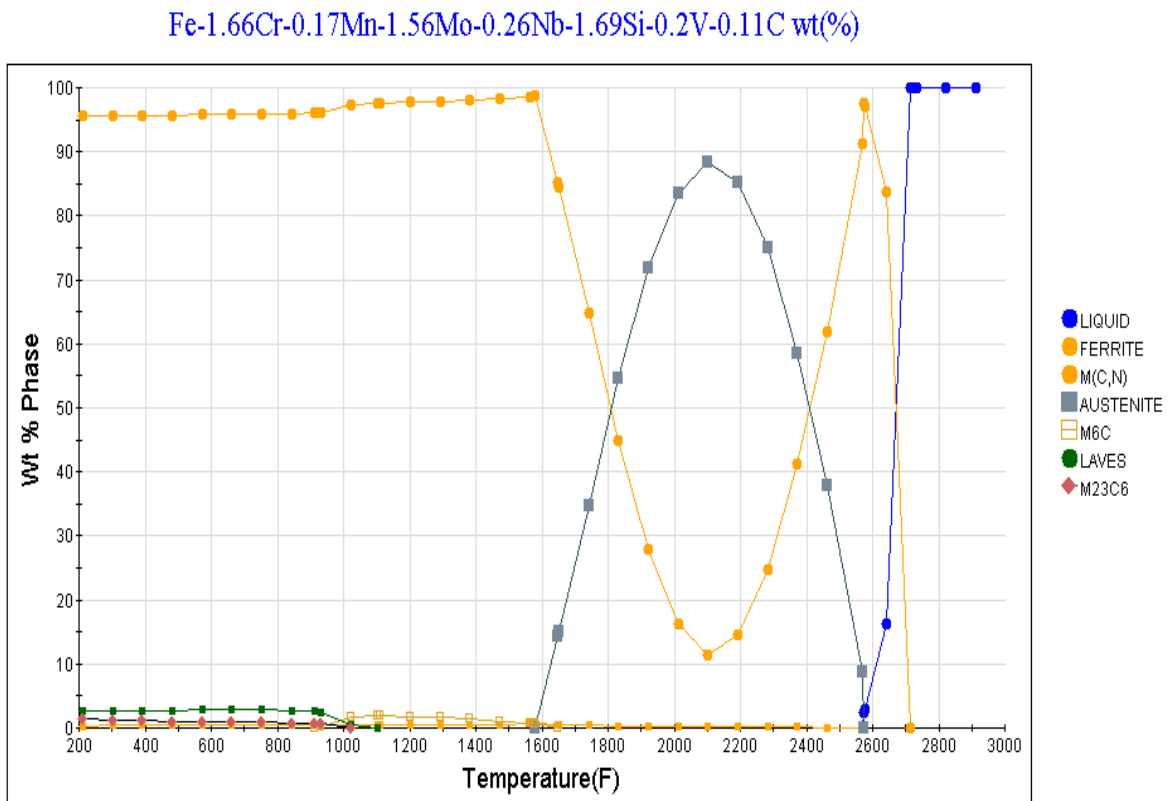

Figure 5. CALPHAD generated diagram showing the temperature-phase relationships of the FSLA.

Both continuous and batch heat treatments were performed on the samples. For the continuous process, a high temperature Abbott continuous-belt furnace was used at the indicated temperature for 30 minutes in an atmosphere of 95 vol.% nitrogen/5 vol.% hydrogen. Batch heat treatments were performed in either a vacuum or a standard box furnace at the indicated temperature in an atmosphere of 95 vol.% nitrogen/5 vol.% hydrogen.

Five tensile specimens (flat, unmachined dogbones) were evaluated for each heat treated condition. Rockwell (HRA) hardness was measured on the samples in accordance with MPIF Standard 43.[10] The densities of the sintered bars were estimated following MPIF Standard 42[11] and tensile testing followed MPIF Standard 10.[12]

Several metallographic tests were performed on sections taken from the tested samples. Representative samples were selected, and sections removed for examination in both the as-polished and etched conditions. The sections were mounted, ground, and polished using standard metallographic techniques.

Revealing the microstructure was accomplished using several chemical etching solutions, with the choice of etchant dependent on the heat treated condition of the sample, the microstructure, and the information desired from the examination.

Nital etchants at two concentrations, 2 or 5 vol.% (nitric acid [HNO_3] + ethyl alcohol [C_2H_5OH]), or a combination of 2 vol.% nital and 4 wt.% picral (4 g picric acid [$C_6H_3N_3O_7$] + 100 ml ethyl alcohol) was often used to reveal the basic microstructures, including the grain/feature size, the transformation products present and their locations. In addition, a stain (tint etchant) was used to visually separate the various microstructural constituents by color with a two-step pre-etch/stain procedure. To reveal the microstructure for analysis using color, the as-polished surfaces were lightly pre-etched with a short immersion in Vilella's Reagent (5 ml hydrochloric acid [HCl] + 1 g picric acid + 95 ml ethyl alcohol), rinsed with warm water, and dried with a flow of filtered compressed air. In the second step, the pre-etched samples were immersed in a freshly prepared solution of 10 g sodium metabisulphite ($Na_2S_2O_5$) in 100 ml deionized water. While immersed, a chemical layer was deposited on the sample surface and, as the thickness of the layer increased, the appearance of the surface changed from highly light reflective in the pre-etched condition, to tan, progressing to blue. When the desired color and layer thickness were attained, the samples were removed from the solution, rinsed with warm water, ethyl alcohol, then blown dry with filtered compressed air.[13-15] In this study, the staining time was varied to present two appearances, with one displaying more variation in color due to the variations in microstructures.

The stain or tint etch separated the transformation products, martensite and/or bainite, and two ferrites by depositing the chemical layer that interfered with reflection of the microscope light from the sample surface. The light interference produces colors, with the changes in color caused by the local thickness of the layer. The relative layer thickness is determined by local chemical composition, grain orientation, and microstructure. In some cases, such as with short deposition time, it might be minimal and not produce a variation in color, although still revealing the microstructure. In others, martensite and bainite appear as dark, brownish or nearly black, and the ferrites are generally combinations of tan, yellow, and blue. In some areas containing color, the colors seen during metallographic examination might be the same, but the depth of color different, indicating a variation in local chemical composition.

Both light optical microscopy (LOM) and SEM were used in the analysis. For the LOM examination, either a Leica MEF4 or Nikon Epiphot 200 metallograph was used. Both systems were equipped with digital imaging and image analysis software from Clemex Technologies Inc., Longueuil, Quebec, Canada. Microindentation hardness testing of the individual phases was performed using a Vickers indenter at 50 or 100 gf following ASTM E384.[16]

LOM testing also included a quantitative estimation of the constituent content in the etched or stained samples using a systematic manual point count. In this procedure, an overlay of equally spaced X-Y grid points was superimposed on multiple live images of the microstructure and the grid points coinciding with the individual features of interest counted. The total counted points for each constituent were then divided by the total number of points applied to the sample and this value was the estimated area fraction of the counted features. Since the section prepared for analysis is representative of the sample volume, this area fraction is equivalent to the volume fraction. The image magnification, point spacing, and

number of analyzed fields were determined by the scale and percentage of the features in the microstructures.[17,18]

A JEOL JSM-IT700HR FESEM was used for both imaging and estimating the local chemical composition of the various constituents in the microstructure. Both SEI and backscattered electron images (BEI) were used to document the microstructures and the chemical analyses were performed using an integrated energy dispersive spectrometer (EDS). In most cases, the etched or stained surfaces were used for the analyses. When estimating the local chemical compositions, EDS spectra were collected using an accelerating voltage of 15 keV for 60 seconds live acquisition time, with the probe current set for ≈20% dead time and, unless otherwise stated, the region chosen for analysis was rectangular in shape, with an area of approximately 20 μm^2. Standardless calculations of the acquired data were made using the JEOL EDS software with ZAF correction.

RESULTS AND DISCUSSION

Figure 6 gives an indication of the versatility of this AM alloy by looking at the combination of mechanical properties that were obtained using multiple intercritical annealing (heat treatment) cycles. It shows the comparison of two AM processed samples, MBJ and LPBF, with established wrought mechanical properties. The wrought properties are represented by the red circles and line, with the value following the DP designation the estimated ultimate tensile strength (UTS) in MPa. The MBJ properties are displayed in blue and the LPBF in green. The results from both AM processes confirm the ability of these techniques to exceed the performance of the well-established wrought DP steels. In addition, the alloy and process development are being expanded to using carbon contents higher than 0.12 wt.% with the FSLA composition and creating additional intercritical annealing cycles. Preliminary testing in the AM areas have shown the same promising trends of higher comparative performance like what is displayed in Figure 6.
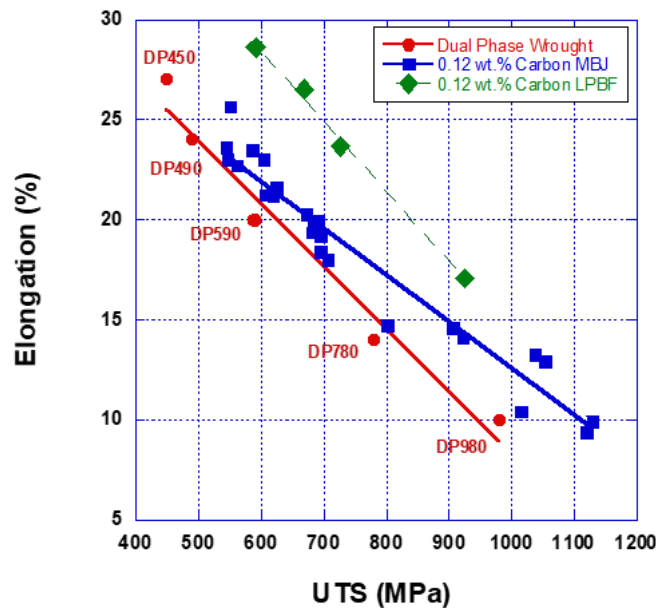

Figure 6. The comparison of UTS and Elongation of the MBJ and LPBF samples compared with the traditional wrought DP steels.

The primary reason for the multiple performance levels is control of the microstructure through the heat treatment cycles. By altering the intercritical annealing temperature, the ferrite:austenite ratio is controlled through a partitioning of the alloying elements, with the compositions of austenite and ferrite changing with temperature. The subsequent method of cooling then determines the amount of ferrite present at room temperature and whether the austenite transforms to martensite or bainite.[19-27] Selected images showing microstructures from a MBJ heat treating experiment are shown in Figure 7, with the annotated intercritical annealing temperatures included in three colors. These colors are the same as the dashed colored lines used in the CALPHAD equilibrium phase graph to show estimates of the two high temperature phases during intercritical annealing. As can be seen in the three photomicrographs, the proportion of the dark bainitic and light ferritic areas changes as the intercritical annealing temperature changes, reflecting the alteration in alloy distribution and a local change in hardenability.
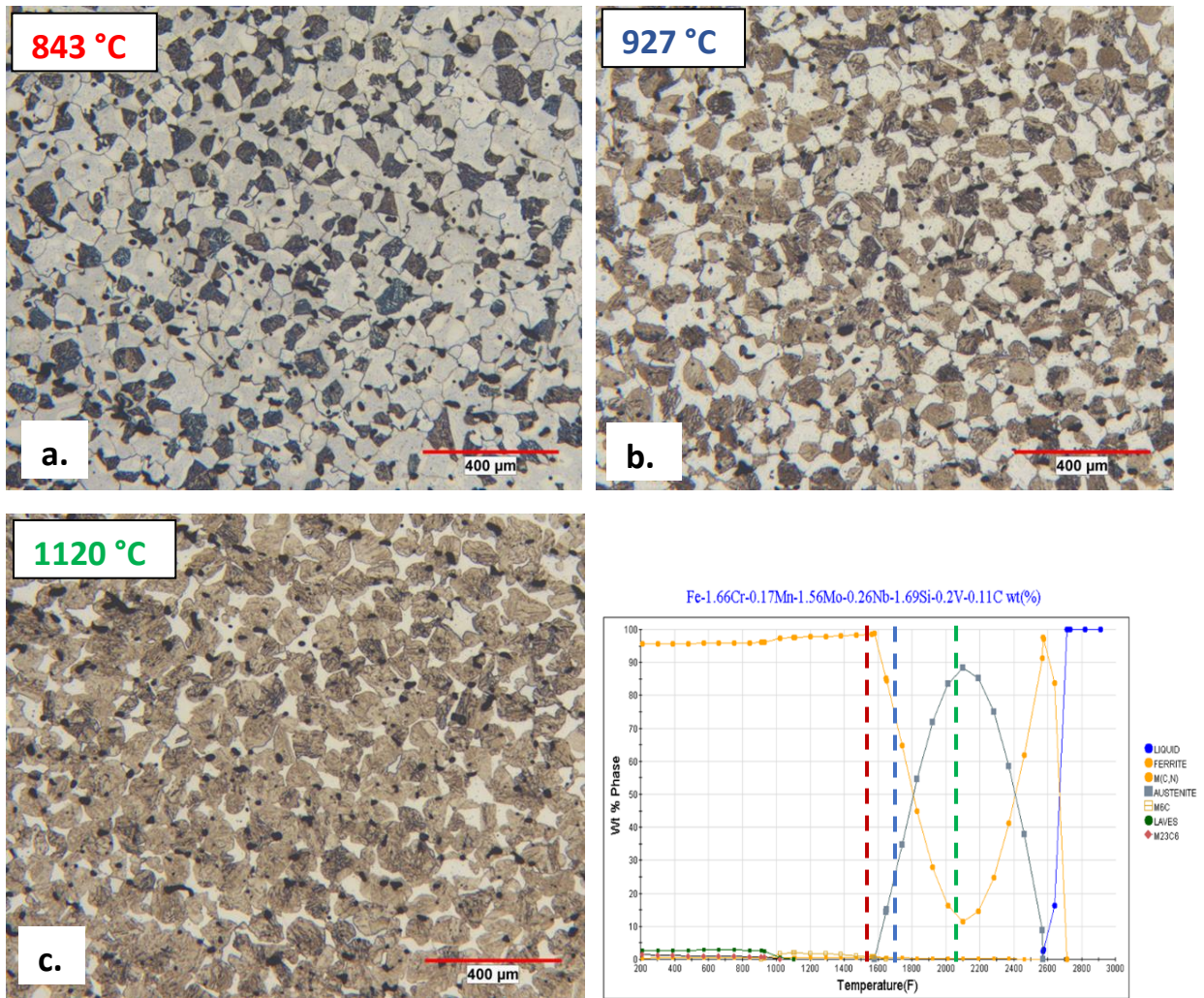
All images; LOM, Vilella's Reagent then 10 wt.% $Na_2S_2O_5$

Figure 7. FSLA intercritically annealed at 843 °C (1550 °F), 927 °C (1700 °F), and 1120 °C (2050 °F) showing the ferrite as the featureless whitish grains and the bainite as the textured browish areas.

As discussed earlier, the four manufacturing methods are separated into two groups. One where the original processing is in the solid state (MBJ and MIM) and the other where samples undergo melting (LPBF and L-DED). The solid-state group must be sintered for particle bonding and densification, while

the samples undergoing melting densify upon solidification. The difference in thermal history also results in completely different pre-intercritical anneal microstructures, as can be seen in Figure 8, which is the printed, then sintered MBJ sample compared with the L-DED as-built sample.

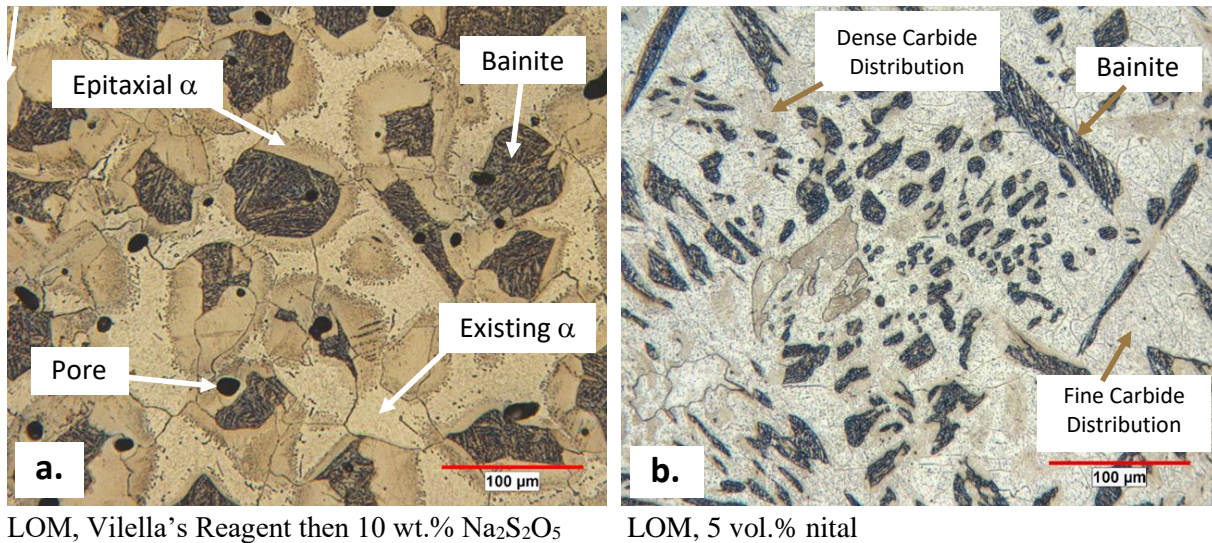LOM, Vilella's Reagent then 10 wt.% $Na_2S_2O_5$ LOM, 5 vol.% nital

Figure 8. FSLA in the as-sintered MBJ condition (a.) and as-built using L-DED (b.)

The as-sintered MBJ photomicrograph in Figure 8a shows the microstructure to be a combination of dark bainitic areas, a small percentage of smooth pores, and two tannish regions that are both ferritic. In this example, where the sample has not undergone intercritical annealing, the two ferrites are formed at different times in the sintering cycle. One is formed at the sintering temperature by partitioning of the alloying elements and the other during cooling. In Figure 8b, the as-built L-DED microstructure resembles more of a solidification structure compared with the as-sintered microstructure in Figure 8a. It appears to be a combination of columnar-type regions of bainite (bluish in color), dense areas of carbide precipitates in ferrite (darker tan), and a finer distribution of carbides in ferrite (lighter tan).

As mentioned above, the multiple ferrites observed in Figure 8a can form during both sintering and intercritical annealing. The ferrite created at the elevated temperature during either sintering or annealing is stable at room temperature and known as existing or old ferrite. In Figure 8a, it is the lighter tan of the two ferrites. As the sample cools from either temperature, the second ferrite forms unless the sample is rapidly cooled or quenched. Known as epitaxial or new ferrite, it is formed through layer-by-layer growth of the former austenite onto the existing ferrite grain. The epitaxial ferrite has the same crystal structure and orientation as the ferrite crystal on which it grows, although the alloy content is greater since the substitutional alloying elements do not have sufficient time to partition into the austenite before transformation occurs. However, the highly mobile interstitial carbon atoms are forced from the epitaxial ferrite as the growth front progresses and may precipitate as carbides as the carbon content increases at the ferrite-austenite boundary. It should also be recognized that no grain boundary is created between the existing and epitaxial ferrites even though they differ in chemical composition. In Figure 8a, it is the darker shade of tan representing the two ferrites and is usually in contact with the martensite or bainite since it was formed from the same austenite that transformed to the harder transformation product. The epitaxial ferrite is an extension of the existing ferrite within the same grain.[28-33]

Although not shown in Figure 8, the as-sintered MIM sample is similar to the MBJ and the LPBF is similar to the L-DED. These are starting microstructures for the intercritical annealing and, because the microstructures are remarkably different, the solid and liquid state processed samples may not respond in the same manner to elemental partitioning with the same intercritical annealing conditions. Adjustments to the annealing cycle may be needed to develop the same two-phase microstructure if required.

In the following several figures, images from two intercritical annealing cycles were chosen from a large array of experiments to illustrate the similarities and differences between the four manufacturing methods by examining the amount and morphology of the resulting transformation products. Figure 5, the equilibrium phase graph, should be revisited to review the predicted ratio of phases present at selected temperatures. In this comparison, one cycle was intended to produce a highly ferritic microstructure. In it, the samples were heated to 1200 °C (2200 °F) for one hour to redistribute the alloying elements and form the maximum amount of austenite, then the temperature was reduced to 800 °C (1475 °F) and held for 2 hours to create the high ferrite percentage before cooling. The second temperature cycle was intended to produce a highly bainitic microstructure, where the samples were heated to 1200 °C (2200 °F), to maximize the amount of austenite, held for 8 hours, then cooled. Cooling after both heating cycles was by gas quenching.

The four pairs of etched/stained LOM photomicrographs in Figures 9 through 12 compare the microstructures from the four manufacturing methods after the ferrite intercritical anneal. This heat treatment produces a lower strength but highly ductile microstructure. Two magnifications were used for each pair of images to allow for a direct comparison of the microstructural features between the manufacturing methods. In each pair, the left image was acquired at a lower magnification and a higher magnification shown on the right to provide greater detail of the microstructure. The same pre-etch/tint etch procedure was used with the immersion time for the tint etch adjusted to produce the interference colors. The variation in color is due to variations in chemical composition and possibly grain orientation. The yellowish regions are higher in alloy content compared with the lighter blue, with the darkest blue probably the lowest.

The overwhelming majority of the microstructures in the four figures is ferrite with a distribution of fine carbide precipitates. The exception is possibly the leanest alloyed areas showing as the darkest blue. The precipitation of the carbides is caused by the change in crystal structure from austenite at the higher temperature, where the solubility of carbon is high, to ferrite at the lower temperature, where the solubility of carbon is considerably lower. The amount of bainite or martensite is near or below 1 vol.% in all cases, with several specific grains containing martensite, highlighted with arrows in the higher magnification images.

During the two-step anneal, the elements in the higher alloyed regions of bainite or martensite diffuse into the sample volume using the grain and interface boundaries as the locations where diffusion and transport occur first. These regions in the MBJ and MIM samples, Figures 9 and 10, appear as a continuous yellowish network through the image area due to the starting microstructure like what was seen in Figure 8a. Specifically, these are the locations where the bainite and epitaxial ferrite diffused from the as-sintered microstructure. Also, while the microstructures are almost totally ferritic, it appears no epitaxial ferrite is present, and all the ferrite is a product of diffusion and the change in crystal structure at the annealing temperature but not epitaxial growth.
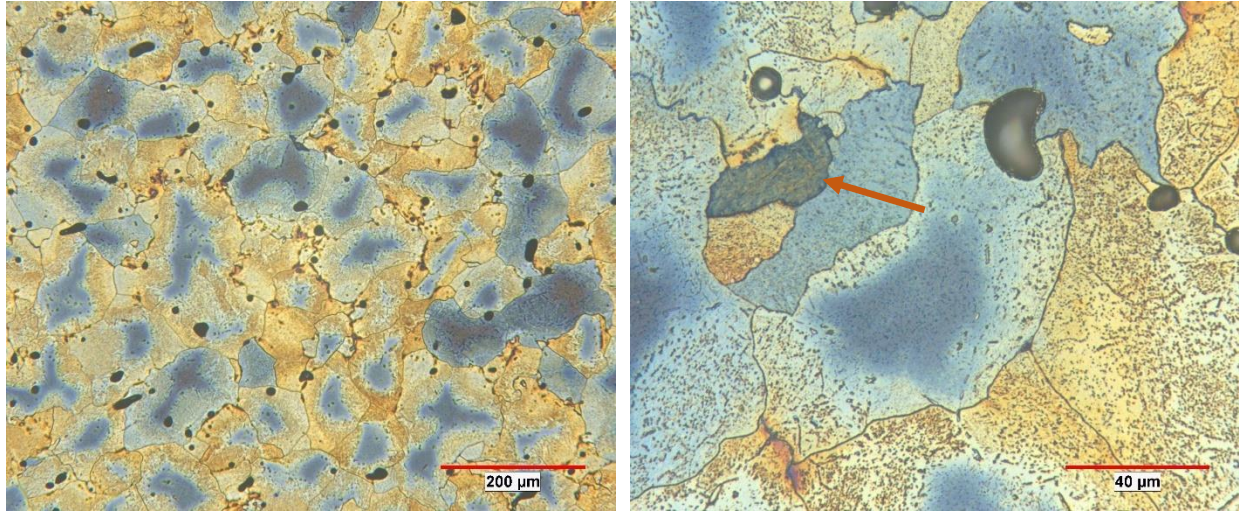
LOM, Vilella's Reagent then 10 wt.% $Na_2S_2O_5$

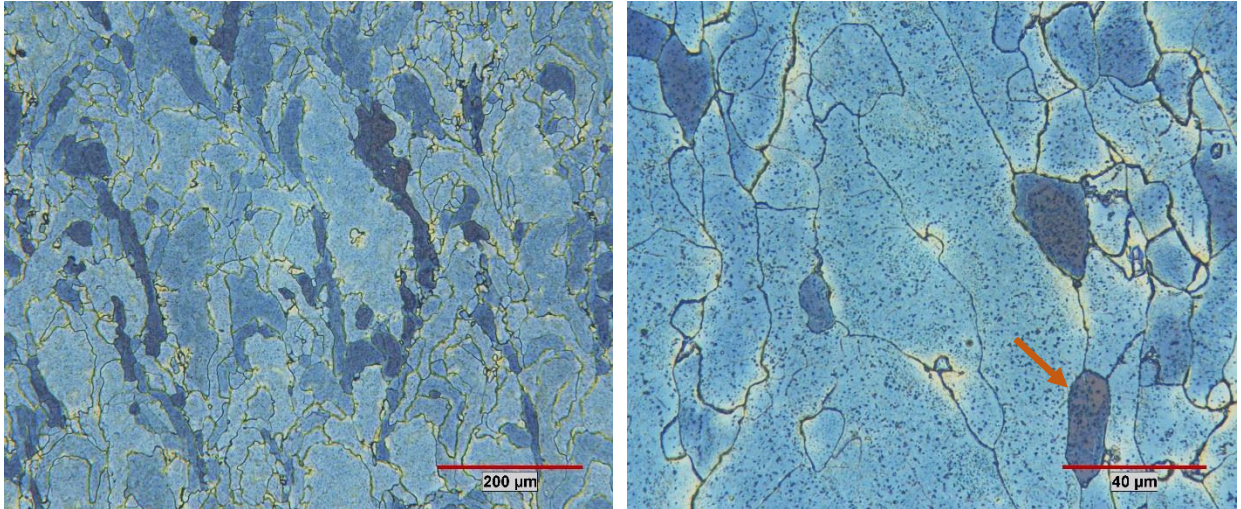Figure 9. MBJ processed samples intercritically annealed using the two-temperature ferrite process.
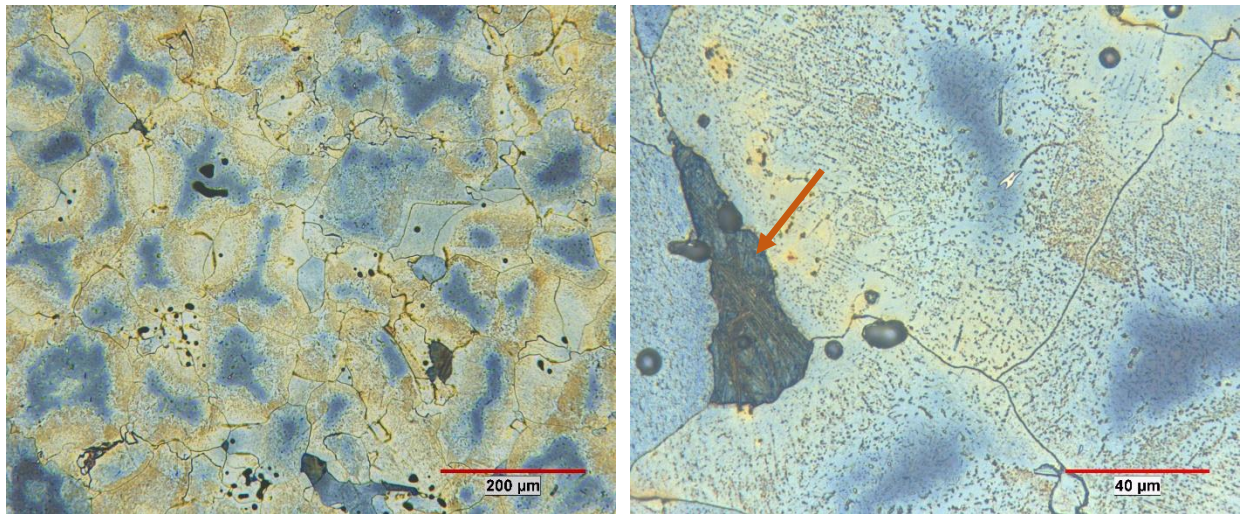
LOM, Vilella's Reagent then 10 wt.% $Na_2S_2O_5$

Figure 10 MIM processed samples intercritically annealed using the two-temperature ferrite process.

The LPBF and L-DED photomicrographs in Figures 11 and 12 also show a primarily ferritic microstructure with a distribution of fine carbide precipitates. However, there are significant differences in these microstructures compared with the solid-state processed samples. Both pairs of images in these figures show directionallity to the grain structure that was caused by solidification. Additionally, the amount of yellowish, higher alloyed regions are distinctly different in comparison. The LPBF sample shows only small localized areas with the lighter stain and the L-DED has a mottled appearance, probably also due to solidification and the locations of both the higher alloyed martensite/bainite and the dense regions of fine carbide precipitates. In both samples, the evidence of solidification is still visible. The lack of epitaxial ferrite with the solidified samples looks to be the same as the two solid-state samples. Again, formation of ferrite appears to be from diffusion and the change in crystal structure rather than epitaxial growth from the existing ferrite grains.

LOM, Vilella's Reagent then 10 wt.% $Na_2S_2O_5$

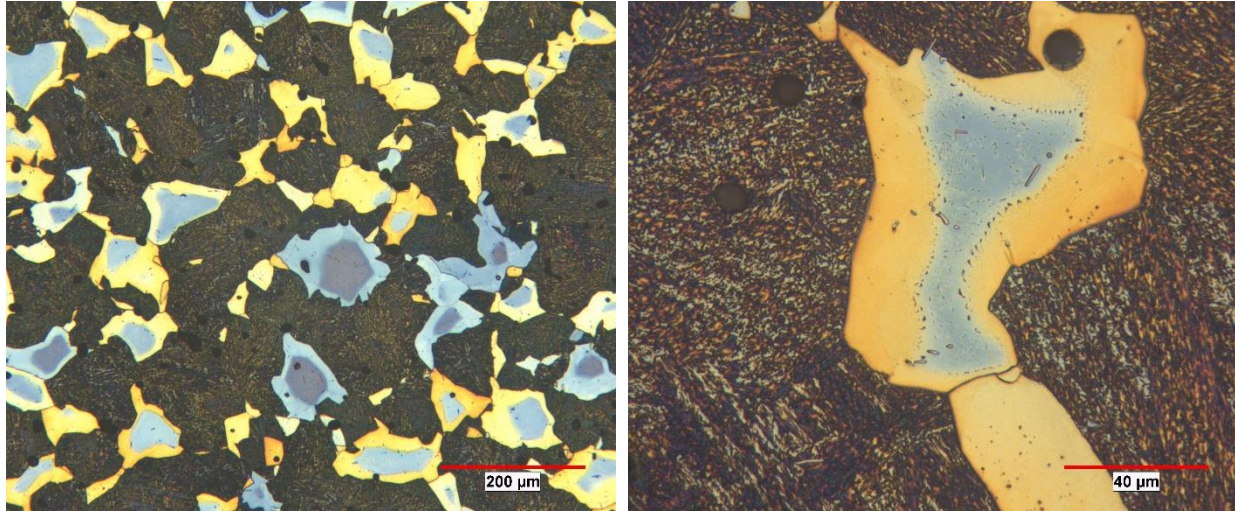Figure 11. LPBF processed samples intercritically annealed using the two-temperature ferrite process.
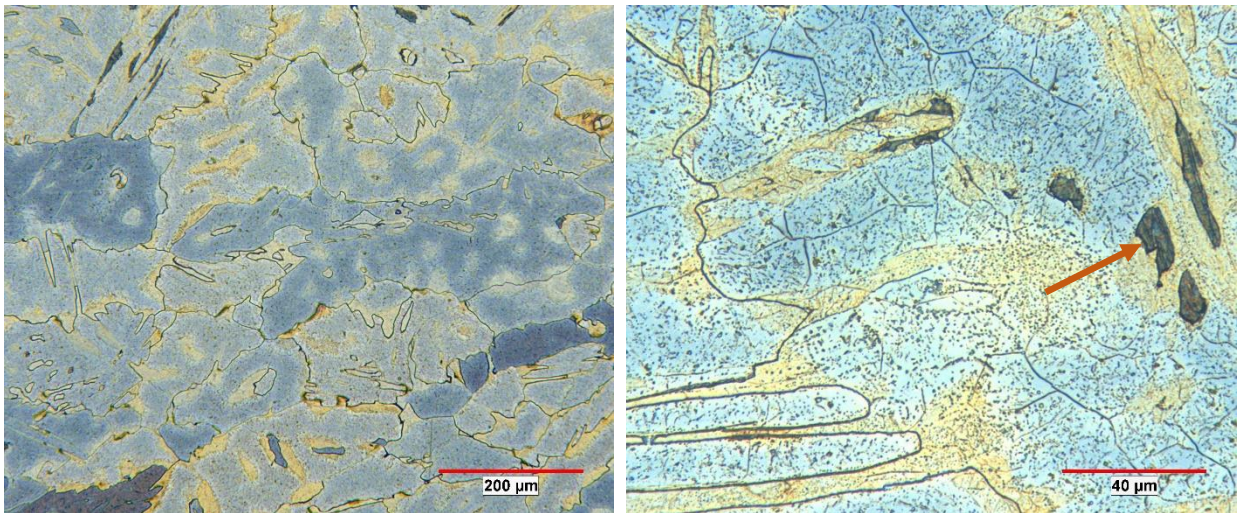
LOM, Vilella's Reagent then 10 wt.% $Na_2S_2O_5$

Figure 12. L-DED processed samples intercritically annealed using the two-temperature ferrite process.

Intercritical annealing with the 8-hour soak time at 1200 °C (2200 °F) also produced two groups of microstructures that were significantly different in comparison. Again, the group-related differences were attributed to the original solid and liquid-state processing. These samples contain a substantially higher percentage bainite and are stronger, but less ductile than the samples containing the higher volume percent ferrite. Figures 13 and 14, the MBJ and MIM samples, showed remarkable similarity in their microstructures. The percentages of bainite and ferrite, both existing and epitaxial, appear similar in amount and morphology. Coloring of the phases in the images are also quite similar, with bainite as the dark brown and the ferrites as blue and yellow. Separation between the two ferrites is distinct and the colors or shades of color show clearly which constituent is present. In the two higher magnification images, the existing ferrite is light blue, with the boundary between the two ferrites decorated with small carbide precipitates. Inside the existing ferrite are carbide precipitates. In comparison, the epitaxial

ferrite is generally yellow in color and bounded on one side by the existing ferrite and bainite on the other. The population of carbide precipitates in the epitaxial ferrite is also less dense than what is visible in the existing ferrite. As mentioned previously, no grain boundary is present between the two ferrites. It should be mentioned that the ferrite grains in the low magnification images consisting of only the blue stain still display the difference in chemical composition between the existing and epitaxial ferrite, however the difference is in the depth of color. In these cases, the lighter blue epitaxial ferrite is located between the existing ferrite (darker blue) and bainite and it is higher in alloy content compared with the existing ferrite.

LOM, Vilella's Reagent then 10 wt.% $Na_2S_2O_5$

Figure 13. MBJ built samples intercritically annealed using the single temperature, high bainite process.
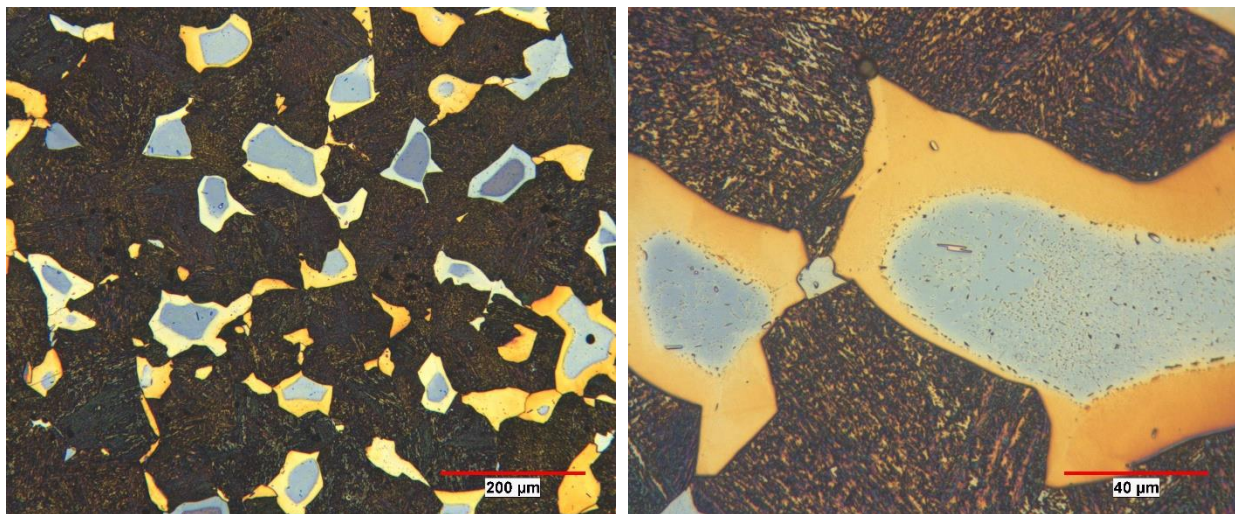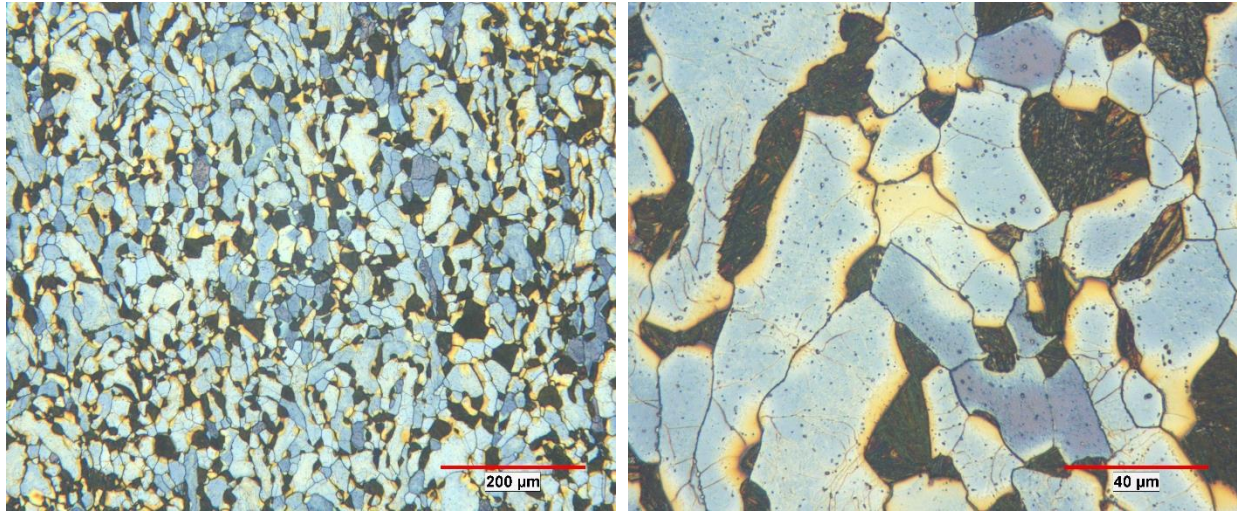

LOM, Vilella's Reagent then 10 wt.% $Na_2S_2O_5$

Figure 14. MIM samples intercritically annealed using the single temperature, high bainite process.

The images from the L-DED and LPBF are shown in Figures 15 and 16. They are substantially different than both the MBJ and MIM samples and to each other. Again, this can be explained by the thermal

history of the samples and solidification. The amount of bainite is much lower due to the local alloy contents and the two ferrites are not as well-defined as in the MBJ and MIM samples. The size, shape, distribution, and directionality of the individual features also appear to be remnants from the as-solidified microstructure. Epitaxial ferrite looks to be present in the L-DED sample, but it could be argued the yellowish regions in the LPBF sample might be caused by diffusion from a higher alloyed feature and not epitaxial growth. Both the grain size and the distribution of carbide precipitates are of particular interest in these samples. The sizes of both the ferrite grains and transformation product differ greatly comparing the two samples and the fine carbides appear to be precipitated in both ferrites, which might indicate that the precipitation occurred during cooling from the melting temperature.

LOM, Vilella's Reagent then 10 wt.% $Na_2S_2O_5$

Figure 15. LPBF built samples intercritically annealed using the single temperature, high bainite process.
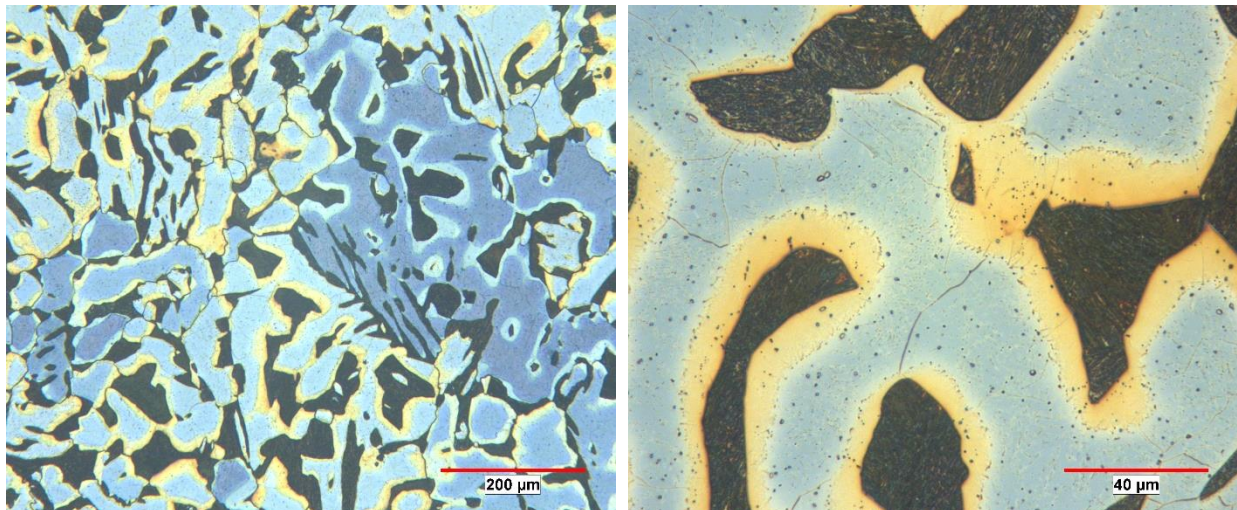
LOM, Vilella's Reagent then 10 wt.% $Na_2S_2O_5$

Figure 16. L-DED built samples intercritically annealed using the single temperature, high bainite process.

Quantitative estimates of the phase percentages from the high percentage bainite intercritical anneal were made using a systematic manual point count, with the results included in Table II. These percentages seem to agree with the etched/stained images in the previous figures. While all four sample groups were intercritically annealed at the same time, the phase ratio between the solid and liquid state processed groups is different, although the overall chemical compositions are the same. In comparison with the prediction in Figure 5, the samples processed in solid-state are remarkably close to the estimated amount but those processed through melting are not. Finally, the yellowish areas in the LPBF sample were originally counted as epitaxial ferrite, however it is not clear these regions are epitaxial ferrite and may be caused by diffusion and not growth. Consequently, this small value could be added to the existing ferrite estimate if needed.

Table II.
Estimated Microstructural Composition of the 1200 °C, 8 Hrs. Samples

	Martensite and/or Bainite	Existing Ferrite	Epitaxial Ferrite
MBJ	83	4	13
MIM	78	5	17
LPBF	21	73	6*
L-DED	30	52	18

*Although this ferrite is similar in color to the epitaxial ferrite in other samples, it is uncertain it is epitaxial ferrite, and the color may be caused by diffusion from a higher alloyed feature and not epitaxial growth.

The thermal processes of sintering and intercritical annealing all contribute to the partitioning of the alloying elements between the phases. These contributions to redistributing the elements usually do not reach the estimated equilibrium compositions because the times at temperature are insufficient and the mobility of the substitutional alloying elements are different. However, examining the microstructures from the 1200 °C (2200 °F) samples showed the three microstructural components, bainite and the two ferrites, were present in all except possibly the LPBF sample, which was likely missing the epitaxial ferrite. Consequently, chemical analyses using EDS were performed on samples from each manufacturing method to look for trends in the alloy distribution. Table III describes some of the findings from this part of the study and these comments are relevant for all manufacturing methods.

Table III.
Partitioning of the Alloying Elements

Element	Observation
C	Highest in bainite
Si	Highest in existing ferrite, lowest in bainite
V	Relatively uniform, although slightly lower in the bainite
Cr	Highest in the epitaxial ferrite; lowest in the existing ferrite
Mn	Relatively uniform
Nb	Highest in the bainite
Mo	Highest in the existing ferrite; bainite and epitaxial ferrite virtually equal

Table II shows that the epitaxial ferrite occupies a substantial volume percent of the samples and in Table III, as having a similar chemical composition to the bainite since it was grown from the austenite as the sample experienced cooling. Being more-heavily alloyed than the existing ferrite, the properties of this phase are different. Microindentation hardness measurements on the epitaxial ferrite are in the range of 40 to 80 HV 0.1 harder than the existing ferrite. In addition, being a harder phase also implies it is stronger than the existing ferrite, although at a cost of a slight reduction in ductility.

As discussed above, the cooling rate from sintering, solidification, and intercritical annealing can result in the formation and growth of the epitaxial ferrite unless the sample is quenched or cooled rapidly. As the temperature of the sample in the two-phase ($\alpha + \gamma$) region decreases during cooling, the proportion of austenite and ferrite changes with an increase in the ferrite content and a corresponding decrease in austenite. However, the rate at which this happens is too rapid for partitioning of the substitutional elements to the equilibrium chemical compositions of austenite and ferrite. Consequently, the new epitaxial ferrite has a more highly alloyed chemical composition compared with the existing ferrite. In addition, the solubility of carbon in the austenite (FCC) is much greater than in ferrite (BCC) and, being more mobile than the substitutional elements, it is forced from the austenite as the epitaxial ferrite growth front progresses. An example of this growth is seen in the two Figure 17 images of a MBJ sample that had been intercritically annealed at 1200 °C (2200 °F) for the 8 hr. hold time.
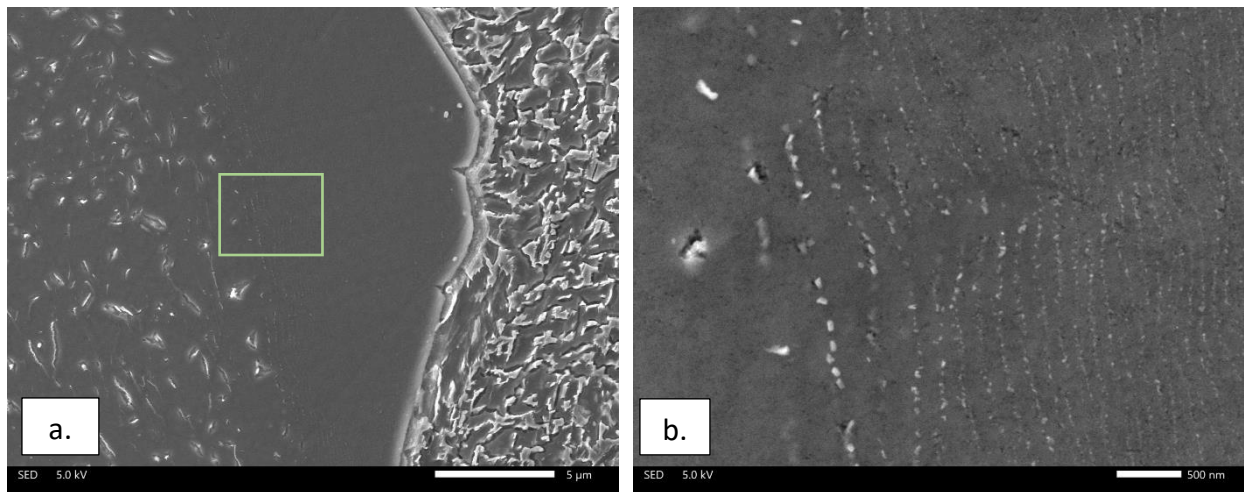
SEM-SEI, Vilella's Reagent then 10 wt.% $Na_2S_2O_5$

Figure 17. MBJ sample intercritically annealed at 1200 °C (2200 °F) for the 8 hr. hold time. Scale bar for the left (a.) image is 5 µm and 500 nm for the right (b.) image.

In the lower magnification SEI on the left (Figure 17a), the bainite occupies the right side of the image and the left side is the existing ferrite, with the carbide precipitates appearing as the small thin white features. Between the two is the epitaxial ferrite, which is smooth and relatively featureless. Since the epitaxial ferrite grows from the edge of the existing ferrite, the region inside the annotated rectangle was selected for a more detailed examination from the origin of growth, moving toward the bainite. Figure 17b, the area inside the rectangle, shows the microstructure at a higher magnification and effects of this growth. With the initial growth layer toward the left side, it appears contour layers of carbide precipitates are formed as the growth progresses from left to right. As epitaxial growth proceeds and the austenite is converted to ferrite, the carbon solubility in the ferrite is reduced and forced into the remaining austenite

toward the right. This creates a carbon-enriched boundary layer where the carbon content may be too high to remain in solution. Consequently, the boundary between the newly formed epitaxial ferrite and the remaining austenite appears to be decorated with this layer of precipitates. This process continues with the layer-by-layer precipitation of the small carbides until the austenite transforms to bainite.[34-35] These carbides may be high in Cr, a carbide former present in the austenite and measured as having the highest concentration in the epitaxial ferrite (see Table III). The presence of the carbides also removes both carbon and the carbide forming elements from alloying, thus making the hardenability of the austenite lower.

CONCLUSIONS

The experiments with the AM methods and MIM have demonstrated the likelihood that, although the FSLA was designed for use with MBJ, it also can be used as the feedstock for the other manufacturing methods. It is clear the intercritical annealing cycles used to generate the variable microstructures responsible for the range of mechanical properties are not universal and modifications are required as the manufacturing method is changed. As seen with the photomicrographs in this document, the constituents in the microstructure are generally the same after annealing, although their scale, distribution, and orientation may be different. The effects of the pre-intercritical anneal microstructure also have a profound impact on the final dual phase microstructure, although much of this can be overcome by well-designed thermal processing to produce parts with predictable performance. Accomplishing this can make the FSLA economically more attractive by using a greater percentage of the overall particle size distribution, which equates to a lessening of the manufactured part cost.

REFERENCES

1. A New Global Formability Diagram, WorldAutoSteel, https://ahssinsights.org/blog/a-new-global-formability-diagram/
2. C. Schade, T. Murphy, K. Horvay, A. Lawley, and R. Doherty, "Development of a Free Sintering Low Alloy (FSLA) Steel for the Binder Jet Process", *Advances in Additive Manufacturing with Powder Metallurgy – 2021*, compiled by S. Atre and S. Jackson, Metal Powder Industries Federation, Princeton, NJ, 2021, part 7, pp. 287-306.
3. C. Schade, T. Murphy, and K. Horvay, "Microstructure and Mechanical Properties of FSLA Steel Produced by the Binder Jet Process", *Advances in Additive Manufacturing with Powder Metallurgy – 2022*, compiled by A. Bose and J. Sears, Metal Powder Industries Federation, Princeton, NJ, 2022, part 6, pp. 343-355.
4. L. Donoho, D. Webster, T. Murphy, and C. Schade, "Microstructure and Mechanical Properties of FSLA Steel Produced by the Metal Injection Molding", *Advances in Powder Metallurgy and Particulate Materials – 2022*, compiled by P. Hauck and T. McCabe, Metal Powder Industries Federation, Princeton, NJ, 2022, part 4, pp. 169-179.
5. R.M. German, *Sintering Theory and Practice*, First Edition, 1996, John Wiley & Son, New York, NY.
6. T.M. Puscas, A. Molinari, J. Kazior, T. Pieczonka, and M. Nykiel, "Sintering Transformations in Mixtures of Austenitic and Ferritic Stainless Steel Powders", *Powder Metallurgy*, 2001, Vol. 44, No. 1, pp. 48-52.

7. R.I. Sands and J.F. Watkinson, "Sintered Stainless Steels I.- The Influence of Alloy Composition Upon Compacting and Sintering Behaviour", *Powder Metallurgy*, 1960, Vol. 3, No. 5, pp. 85-104.

8. N.B. Shaw and R.W.K. Honeycombe, "Some Factors Influencing the Sintering Behaviour of Austenitic Stainless Steels", *Powder Metallurgy*, 1977; Vol. 20, No. 4, pp. 191-198.

9. ArcelorMittal, Dual phase steels, Chemical composition, Cold rolled steel, https://automotive.arcelormittal.com/products/flat/first_gen_AHSS/DP

10. MPIF Std. 43, "Method for Determination of the Rockwell Apparent Hardness of Powder Metallurgy (PM) Products", *Standard Test Methods for Metal Powders and Powder Metallurgy Products,* Metal Powder Industries Federation, Princeton, NJ, 2022.

11. MPIF Std. 42, "Method for Determination of Density of Compacted or Sintered Powder Metallurgy Products", *Standard Test Methods for Metal Powders and Powder Metallurgy Products,* Metal Powder Industries Federation, Princeton, NJ, 2022.

12. MPIF Std. 10, "Determination of the Tensile Properties of Powder Metallurgy (PM) Materials", *Standard Test Methods for Metal Powders and Powder Metallurgy Products,* Metal Powder Industries Federation, Princeton, NJ, 2022.

13. M. Mazinani and W.J. Poole, "Effect of Martensite Plasticity on the Deformation Behavior of a Low-Carbon Dual-Phase Steel", *Metallurgical and Materials Transactions A*, 2007, Vol. 38A, pp. 328-339.

14. G.F. Vander Voort, *Metallography Principles and Practice*, First Edition, 1984, McGraw-Hill Book Company, New York, NY.

15. G.F. Vander Voort, "Tint Etching", *Metal Progress*, 1985, March, pp. 31-41.

16. ASTM Standard Test Method E384, "Standard Test Method for Microindentation Hardness of Materials", *Book of ASTM Standards*, Vol. 03.01, 2022, ASTM International, West Conshohocken, PA.

17. ASTM Standard Test Method E562, "Determining Volume Fraction by Systematic Manual Point Count", *Book of ASTM Standards*, Vol. 03.01, 2022, ASTM International, West Conshohocken, PA.

18. E.E. Underwood, *Quantitative Stereology*, First Edition, 1970, Addison-Wesley Publishing Company, Reading, MA.

19. A. Bag, K.K. Ray, and E.S. Dwarakadasa, "Influence of Martensite Content and Morphology on Tensile and Impact Properties of High-Martensite Dual-Phase Steels", *Metallurgical and Materials Transactions A*, 1999, Vol. 30A, No. 5, 1193-1199.

20. K. Bräutigam-Matus, G. Altamirano, A. Salinas, A. Flores, and F. Goodwin, "Experimental Determination of Continuous Cooling Transformation (CCT) Diagrams for Dual-Phase Steels from the Intercritical Temperature Range", *Metals*, 2018, Vol. 8, No. 9, 674, https://doi.org/10.3390/met8090674

21. M.C. Chaturvedi and A.K. Jena, "Effect of Intercritical Annealing Temperature on Equilibrium Between Ferrite and Austenite", *Materials Science and Engineering*, 1987, Vol. 94, pp. L1-L3.

22. V. Colla, M. Desanctis, A. Dimatteo, G. Lovicu, and R. Valentini, "Prediction of Continuous Cooling Transformation Diagrams for Dual-Phase Steels from the Intercritical Region, *Metallurgical and Materials Transactions A*, 2011, Vol. 42A, pp. 2781-2793.

23. B. Demir and M. Erdogan, "The Hardenability of Austenite with Different Alloy Content and Dispersion in Dual-Phase Steels", *Journal of Materials Processing Technology*, 2008, Vol. 208, pp. 75-84.

24. A.D. Romig and R. Salzbrenner, "Elemental Partitioning as a Function of Heat Treatment in an Fe-Si-V-C Dual Phase Steel", *Scripta Metallurgica*, 1982, Vol. 16, pp. 33-38.

25. G.R. Speich, V.A. Demarest, and R.L. Miller, "Formation of Austenite During Intercritical Annealing of Dual-Phase Steels", *Metallurgical Transactions A*, 1981, Vol. 12A, pp. 1419-1428.
26. Y.L. Su and J. Gurland, "Strain Partition, Uniform Elongation and Fracture Strain in Dual-phase Steels", *Materials Science and Engineering*, 1987, Vol. 95, pp. 151-165.
27. P. Wycliffe, "Microanalysis of Dual Phase Steels", *Scripta Metallurgica*, 1984, Vol. 18, pp. 327-332.
28. M. Erdogan, "The Effect of New Ferrite Content on the Tensile Fracture Behaviour of Dual Phase Steels", *Journal of Materials Science*, 2002, Vol. 37, pp. 3623-3630.
29. M. Geib, D.K. Matlock, and G. Krauss, "The Effect of Intercritical Annealing Temperature on the Structure of Niobium Microalloyed Dual-Phase Steel", *Metallurgical Transactions A*, 1980, Vol. 11A, pp. 1683-1689.
30. G.S. Huppi, D.K. Matlock, and G. Krauss, "An Evaluation of the Importance of Epitaxial Ferrite in Dual-Phase Steel Microstructures", *Scripta Metallurgica*, 1980, Vol. 14, No. 11, pp. 1239-1243.
31. D.A. Korzekwa, D.K. Matlock, and G. Krauss, "Aging Susceptibility of Retained and Epitaxial Ferrite in Dual-Phase Steels", *Metallurgical Transactions A*, 1982, Vol. 13A, pp. 2061-2064.
32. D.K. Matlock, G. Krauss, L.F. Ramos, and G.S. Huppi, "A Correlation of Processing Variables with Deformation Behavior of Dual Phase-Steels", *Structure and Properties of Dual-Phase Steels*, Edited by R.A. Kot & J.W. Morris, The Metallurgical Society of AIME, Warrendale, PA, 1979, pp. 62-91.
33. M. Sarwar, E. Ahmad, K.A. Qureshi, and T. Manzoor, "Influence of Epitaxial Ferrite on Tensile Properties of Dual Phase Steel", *Materials & Design*, 2007, Vol. 28, pp. 335-340.
34. R.W.K. Honeycombe and F.B. Pickering, "Ferrite and Bainite in Alloy Steels", *Metallurgical Transactions*, 1972, Vol. 3, pp. 1099-1112.
35. H. Mohrbacher, "Principal Effects of Mo in HSLA Steels and Cross Effects with Microalloying Elements", *Proceedings International Seminar in Applications of Mo in Steels*, Beijing, China, 2010, pp. 75-96.